



### CryoEM from Molecular Machines to Cells

Journal:	<i>Nanotechnology</i>
Manuscript ID:	NANO-31723-013.R1
Wiley - Manuscript type:	Standard Article
Date Submitted by the Author:	n/a
Complete List of Authors:	Chiu, Wah
Keywords:	electron, cryomicroscopy, cryotomography, nanomachine, cell
Abstract:	<p>Electron cryomicroscopy (cryo-EM) is an emerging biophysical tool that can be used to determine structures of molecular nanomachines in fully solvated conformations at subnanometer resolutions (&lt;math&gt;\leq 1\text{nm}&lt;/math&gt;). Such cryo-EM maps can reveal long <math>\alpha</math>-helices and large <math>\beta</math>-sheets. In the highest resolution cryo-EM density maps, it is possible to see bulky side chains and trace the C <math>\alpha</math> backbone of molecular subunits within a multi-component nanomachine. Electron cryo-tomography (cryo-ET) is equally powerful because of the unique cellular context in which it can capture and reveal cellular nanomachines. Despite reaching only 4-10 nm resolution, cryo-ET reconstructions are capable of imaging whole cells and distinguishing their molecular components. Both of these methods are complementary to conventional methods of structure determination, including X-ray crystallography and NMR spectroscopy. Hybrid methods that combine these structural techniques with cryo-EM and cryo-ET result in a complete view of nanomachines from atomic detail to their spatial and temporal location within a cell. This chapter will describe the experimental and computational pipeline in cryo-EM and cryo-ET and illustrate their effectiveness with examples from an ion channel, spherical virus, cellular motor and the survey of a complete cell.</p>



# **Electron Cryo-microscopy of Molecular Nanomachines and Cells**

Matthew L. Baker, Michael P. Marsh and Wah Chiu

National Center for Macromolecular Imaging, Verna and Marrs McLean Department of Biochemistry and Molecular Biology, Baylor College of Medicine, Houston, TX 77030 USA

For Peer Review

***Abstract***

Electron cryomicroscopy (cryo-EM) is an emerging biophysical tool that can be used to determine structures of molecular nanomachines in fully solvated conformations at subnanometer resolutions ( $<1$  nm). Such cryo-EM maps can reveal long  $\alpha$ -helices and large  $\beta$ -sheets. In the highest resolution cryo-EM density maps, it is possible to see bulky side chains and trace the  $C\alpha$  backbone of molecular subunits within a multi-component nanomachine. Electron cryo-tomography (cryo-ET) is equally powerful because of the unique cellular context in which it can capture and reveal cellular nanomachines. Despite reaching only 4-10 nm resolution, cryo-ET reconstructions are capable of imaging whole cells and distinguishing their molecular components. Both of these methods are complementary to conventional methods of structure determination, including X-ray crystallography and NMR spectroscopy. Hybrid methods that combine these structural techniques with cryo-EM and cryo-ET result in a complete view of nanomachines from atomic detail to their spatial and temporal location within a cell. This chapter will describe the experimental and computational pipeline in cryo-EM and cryo-ET and illustrate their effectiveness with examples from an ion channel, spherical virus, cellular motor and the survey of a complete cell.

## 1. INTRODUCTION

Genome sequencing projects continue to provide complete genetic descriptions of an ever-increasing number of model organisms [1-4]. Based on our current knowledge, it has been estimated that life depends on 200-300 core biological processes [1]. Individual gene products rarely function independently; to the contrary, large multi-component protein assemblies are more often responsible for complex cellular functions. These assemblies are often dynamic, and in many cases transient. As such, these assemblies are often termed “molecular nanomachines”, capable of carrying out a wide range of functions through often specific and highly intricate interactions [6-10].

Equally as complex as the nanomachines themselves, the individual components can adopt a wide variety of morphologies, functions and interactions. In addressing these complexities, structural genomics seeks to provide a description of all protein folds, where a fold is defined as the three-dimensional (3D) structure of protein that relates the spatial arrangements and connectivity of secondary structure elements, such as  $\alpha$ -helices and  $\beta$ -sheets. As such, the protein fold represents the basic “building block” of much larger and more complex assemblies that carry out biochemical and cellular processes. To date, more than 51,000 individual protein structures are known [2], however far fewer unique folds are known.

It is generally accepted that primary structure, the amino acid sequence of the protein, dictates its 3D structure, or fold. As such, proteins with similar primary sequence likely assume similar folds. However, the converse is not necessarily true; proteins with vastly dissimilar sequence can assume similar folds. Nonetheless, the protein fold is ultimately responsible for the necessary 3D environment for protein function and inter- and intra-molecular interactions. The description of these folds and, in particular their interactions within cellular complexes, is therefore paramount to the understanding of all molecular nanomachines and biological processes.

Electron cryomicroscopy (cryo-EM) is an emerging methodology that is particularly well suited for studying molecular nanomachines at near-native or chemically defined conditions. Cryo-EM can be used to study nanomachines of various sizes, shapes and symmetries, including two-dimensional arrays, helical arrays and single particles [3]. With recent advances, cryo-EM can now not only reveal the gross morphology of these nanomachines, but can also provide highly detailed models of protein folds approaching atomic resolutions [13-17]. This chapter will present the methodology of single particle cryo-EM as well as its potential biomedical applications and future prospects.

Complementary to cryo-EM's application to structural studies of nanomachines is electron cryo-tomography's (cryo-ET) role in depicting the locations and low resolution structures of nanomachines in a 3D cellular environment. The power of cryo-ET comes from its unique ability to observe directly biological nanomachines *in situ* without the need for isolation and purification. This approach has the potential to capture the structural diversity of nanomachines in their milieu of interacting partners and surrounding cellular context.

## 2. STRUCTURE DETERMINATION OF NANOMACHINES AND CELLS

Figure 1 shows a series of typical steps in imaging nanomachines using cryo-EM or cryo-ET. The first steps are common to both techniques; biochemical purification, specimen preservation via rapid freezing and imaging the frozen, hydrated specimens by low dose electron microscopy. The subsequent steps differ for the two techniques but both include image processing to generate a 3D reconstruction, interpreting the 3D volume density together with other biological data and archiving the density maps and models. This chapter will not address how to perform each of the aforementioned mentioned steps, as there are numerous technical works and books that describe them in detail [3, 4]. Rather, we will briefly summarize these steps and their applications to a few examples of molecular nanomachines.

## 2.1. Experimental Procedures in Cryo-EM and Cryo-ET

In principle, most of these steps are rather straightforward and the length of time to start from a highly purified nanomachine to a complete structure can be done in a few days to months. However, just like any experimental method, there can be various hurdles that would require further optimization before a reliable structure can be determined.

### 2.1.1 Specimen Preparation for Nanomachines and Cells

Specimen preparation is a critical step in single particle cryo-EM, which necessarily requires high conformational uniformity while preserving functional activities. In X-ray crystallography, crystallization is a selective process through which only molecules of the same conformations nucleate and crystallize to form a diffracting object. In addition to chemical purification, crystallization also forces the molecules into specific, uniform spatial organization such that diffraction data can be averaged from over billions of molecules in identical conformations. However, cryo-EM experiments image one set of molecules at a time regardless of their conformations and thus possibly represents an ensemble of conformations of the molecules in a single micrograph. In order to obtain the highest possible resolution structures by cryo-EM, it is still necessary to computationally average from several hundreds to tens of thousands of a conformationally homogeneous set of particle images recorded in multiple micrographs. Nevertheless, computational methods are being developed to sort out images of particles with different conformations.

The nature of cryo-ET experiments differs substantially from single particle cryo-EM experiments, and the resolution of the reconstructions is much lower. Contrary to the cryo-EM approach where images of many conformationally uniform particles are merged to yield a 3D model, cryo-ET merges many images of the same specimen target, collected at different angles. With this approach, a reconstruction can be computed from the images of a single cell or nanomachine and so conformational uniformity is not an issue in the most general case. Merging of whole cells or organelles like single particles is not a reasonable goal since uniformity can never realistically be expected; but some subcellular structures may be sufficiently uniform in conformation to warrant merging and

averaging from the 3D tomogram. We consider such an example in our discussion below on the flagellar motor experiments.

### 2.1.2. Cryo-specimen Preservation

Following biochemical isolation and purification, the first step in a cryo-imaging experiment is to embed a biochemically purified nanomachine or cell under well defined chemical conditions in ice on a cryo-EM grid [5]. This freezing process is extremely quick to prevent the formation of crystalline ice and thus produces a matrix of vitreous ice in which the water molecules remained relatively unordered. The spread of the nanomachines on the grid should be neither too crowded such that they would contact each other nor too dilute as to only have a few nanomachines recorded in each micrograph. For cryo-EM, it is preferable to have the nanomachines situated in random orientations to allow sufficient angular sampling needed for the subsequent 3D reconstruction procedure. Ideal thickness of the embedding ice is slightly greater than the size of the nanomachine or cell. Excessive ice thickness is a detriment because it diminishes the signal-to-noise ratio of the images that can be acquired. Ice that is too shallow can be a problem for cryo-ET experiments whereby flattening of the specimen can occur. The capillary forces of the solvent, in the fluid phase just prior to vitrification, can compress the sample; this has been reported in vesicles [6] as well as real cells where a one  $\mu\text{m}$  thick cell can be reduced to 600 nm.[7, 8].

Some specimens are very easy to prepare while others are more difficult, which necessarily means optimization of the specimen preparation is a trial-and-error process. In general, this step—the preparation of the frozen, hydrated specimens, preserved in vitreous ice with an optimal ice thickness—is often a bottleneck. Analogous to the crystallization process in X-ray crystallography, there is no foolproof recipe for optimal specimen preservation. However, a computer driven freezing apparatus has made this step more reproducible and tractable in finding optimal conditions for freezing a given specimen [9].

In principle, the frozen, hydrated specimens represent native conformations as the specimens are maintained in an aqueous buffer. Fixation of the nanomachines in a

specific orientation can occur prior to freezing. Specimen freezing can also be coordinated with a time resolved chemical mixing reaction; prototype apparatuses have been built to perform such a time-resolved reaction [20, 21]. It is conceivable a more sophisticated instrument can be built to allow all sorts of chemical reactions including those that can be light activated. Such an approach would allow cryo-EM to follow the structure variations in a chemical process with a temporal resolution of milliseconds [10].

### **2.1.3. Low Dose Imaging**

Once the sample has been frozen, the entire cryo-EM grid can be inserted into the electron cryo-microscope and imaged with electrons ranging from 100-400 keV. Electrons at these energies will damage the molecules during imaging [3]. Therefore, low dose imaging is necessary to minimize the damage to the specimen before the image is recorded. To maintain the frozen, hydrated specimen in vitreous ice inside the electron microscope vacuum, the specimen is kept at low temperature, typically at or below liquid nitrogen temperature. If the specimen temperature is higher than  $-160^{\circ}\text{C}$ , the vitreous ice undergoes a phase transition to crystalline ice and denatures the nanomachines [5].

From a radiation damage perspective, the advantages and disadvantages of keeping biological specimens at different low temperatures have been studied [22-24]. High quality images have been obtained using liquid helium temperature and have resulted in high-resolution structures of 2D crystals[11, 12], helical arrays[13, 14] and single particles[15, 16] where protein backbone traces were feasible. Imaging specimens at liquid nitrogen temperature has also been used successfully for similar high-resolution structure determination of broad spectrum of specimens [15, 17, 29, 30]. For the case of cellular cryo-ET, it has been suggested that liquid nitrogen is a preferred temperature [17, 18] because of a significant loss of contrast at liquid helium temperature [19].

### **2.1.4. Image Acquisition**

Data collection differs significantly for cryo-EM and cryo-ET. For cryo-EM, images of a field containing multiple, randomly oriented specimens are recorded. Individual particles are recorded only once because of the radiation damage constraints for obtaining the

highest possible resolution information. For cryo-ET, a series of images of the same specimen is acquired as the stage is iteratively tilted over an interval spanning approximately  $130^\circ$ . A typical tilt-series might include one image collected every  $2^\circ$  between  $-65^\circ$  and  $+65^\circ$ . The resolution of the tomographic data is much lower because of the effects of cumulative radiation damage to the specimen throughout the data collection.

For cryo-EM and cryo-ET experiments, images have been traditionally collected on photographic film and subsequently digitized using a high-resolution film scanner. Recent advances in CCD cameras for electron microscopes have made direct digital recording feasible [31-33]. With a modern electron microscope equipped with specialized software for low dose imaging, data collection is relatively simple and can be partially or fully automated [34-37].

## 2.2. Computational Procedures in Cryo-EM and Cryo-ET

The recorded image of a nanomachine is essentially a projection (2D) of its mass density along the path of the irradiating electrons. In order to retrieve its 3D structure, one has to sample the particle in different angular views [20]. For cryo-ET, this sampling is carried out systematically whereby each image in the tilt-series constitutes a separate angular view. With cryo-EM, the varied orientation of particles in the ice naturally provides an angular distribution of views. The number of views required for the reconstruction is proportional to the diameter of the particle and inversely proportional to the desired resolution [21]. Because of the noisy nature of the image and the uneven angular distribution (in the case of cryo-EM) of the views, the actual number of the particles used to calculate a reconstruction at a certain resolution is much higher than the theoretical minimum [22, 40, 41]. Ideally, the particles embedded in the vitreous ice are oriented randomly. However in some cases, the particles tend to assume a preferred orientation with respect to the surface of the embedding ice. This can often be overcome by varying the buffer or solvent (e.g. by adding a small amount of detergent).

### 2.2.1 Image Processing and Reconstruction

During the image processing phase, individual specimen images are aligned with respect to each other and then combined to form a 3D density map [42-44]. For cryo-EM studies, the image processing is an iterative process. There are several image processing packages for single particle cryo-EM, such as EMAN [23], SPIDER [24], IMAGIC [25] and FREALIGN [26]; they are multi-step procedures that can generally be broken into the following steps: identify the locations of each particle, determine and correct the contrast transfer function and damping function for the particle images, classify the images according to their conformational identity and orientation parameters, average the particle images in each classes and 3D reconstruct to produce the final 3D map. Specimen classification, particle averaging and reconstructing the density map are iterated using the previous iteration as a reference. Iteration of these steps continues until no improvement in the 3D density maps is made over the previous cycle of refinement. The final resolution of the map is typically assessed by a parameter called Fourier shell correlation (FSC) in which two maps derived from two independent sets of image data are compared [27]. The FSC essentially measures a similarity and reproducibility of two structures in Fourier space; the final resolution is often determined using the 0.5 criterion.

Alignment and reconstruction differ for cryo-ET experiments. For cryo-ET, the nominal angular assignment is known for each image because the tilt-angle of the stage was recorded for each image of the tilt-series. Higher precision angular assignments must be determined for reconstruction. Alignment processing is frequently simplified by including gold particles in the specimen. The gold particles have strong contrast, even under low dose imaging conditions, and serve as landmarks for registering images with respect to each other [28-30]. Once aligned the images are then recombined directly by a reconstruction algorithm such as weighted back-projection [31, 32]. There are many academically developed processing packages that compute the alignment and reconstruction [33-36]. There is no community-accepted convention for assessing the resolution of tomographic reconstructions, but some statistical approaches have been proposed [37].

### 2.2.2 Structure Analysis and Data Mining

To analyze cryo-EM density maps of large, complex nanomachines, a number of tools have been developed that range from feature detection to domain localization. Perhaps the most well developed set of tools for the analysis of cryo-EM density maps are those designed to fit known crystal or NMR structures to density maps. These tools range from simple rigid-body fitting to complex and dynamic flexible fitting algorithms (reviewed in [50, 51]). Regardless, each of these tools requires that the structures of a known domain or closely related domain are known.

Recent work has also shown that cryo-EM density is sufficient for discriminating good models from a gallery of potential structures [52, 53]. In particular, cryo-EM density has been incorporated as a scoring function in a constrained homology modeling approach [38]. Like the aforementioned fitting routines, this approach relies on the availability of a known structure from which a sequence/structure alignment is produced. In the case where a suitable structural template is not known, a constrained *ab initio* modeling approach has also been developed in which the cryo-EM density can be used directly to screen a large gallery of potential models [39]. While no structural template is needed, this approach is restricted to relatively small (<200 amino acids), single domain proteins.

At subnanometer resolutions, secondary structure elements become visible;  $\alpha$ -helices appear as long density rods, while  $\beta$ -sheets appear as thin surfaces [55-58]. Using a variety of feature detection and computational geometry algorithms, secondary structure elements can be reliably identified and quantified [56, 57, 59, 60]. The spatial description of such elements has been used not only to describe protein structure, but also to infer structure and function of individual protein domains [40, 41].

Until recently, the resolution of cryo-EM density necessitated the use of the aforementioned approaches for understanding macromolecular structure and function. Several cryo-EM structures have now achieved resolutions better than 4.5Å resolution, at which point the pitch of  $\alpha$ -helices, separation of  $\beta$ -strands, as well as the densities that connect them, can be seen unambiguously [13, 14, 15, 17]. In addition to these features, many of the bulky side chains could also be seen. However, it should be noted that these

structures still do not have the resolution to utilize standard X-ray crystallographic methods for model construction. However, several *de novo* models have now been constructed directly from these high-resolution cryo-EM density maps using mostly manual assignment and visualization tools [13, 14, 17].

Annotation of cryo-ET maps is a different process because the goals of tomographic imaging are substantially different. Rather than trying to determine high resolution protein structures, cryo-ET experiments are often focused on how components of cells or nanomachines are spatially organized. Segmentation is a process by which the salient features of the reconstruction of an individual cell or nanomachine are traced. A segmented map hides the noisy data and highlights the structural findings. Tools for segmentation of tomograms include the academic IMOD package [33] and the commercial package Amira (Mercury Systems, Chelmsford, MA). This is a laborious manual process for which no suitable general-purpose automated routine has been advanced (reviewed in [42]). Manual segmentation is applied by annotating one cell or nanomachine at a time. A research study can require the annotation of many cells or nanomachines, which can drastically increase the time required to annotate the results. In cases where there are uniform nanomachines (e.g. ribosomes) present, they can be computationally identified, extracted, and merged to improve the resolution (reviewed in [43])

### 2.3. Data Archival

The result of cryo-EM experiment is typically a 3D density map with multiple domains and/or models used to annotate the structure and function of the molecular nanomachine. In getting to this model, there are multiple intermediate data sets and image processing workflows. Databases, such as EMEN [44] and others [63, 64], work on a laboratory scale and can house the final 3D density maps and model, as well as the original specimen images and all of the intermediate data and processes. The final density map, models and associated metadata can also be deposited in public repositories such as the electron microscopy databank (EMDB) and the protein databank (PDB) [45]. Individual

cryo-EM structures are easily retrieved through accession numbers or IDs directly from publicly accessible websites.

### 3. BIOLOGICAL EXAMPLES

Cryo-EM is a powerful technique in that it can image a large variety of specimens under an equally wide array of conditions. Despite the lack of atomic resolution, these structures can yield unprecedented looks at the structure and function of molecular nanomachines. In the following sections, we describe two very different samples and how cryo-EM has provided us with a unique glimpse into their organization. It should also be noted that each of these samples are complex nanomachines that undergo dynamic structural and functional processes in carrying out their intended functions.

The resolution of cryo-EM models is considerably better than cryo-ET models because the heterogeneous cryo-ET particles are rarely suitable for averaging, and when they are, the average may be the sum of tens to hundreds from extracted tomograms rather than the thousands to millions of asymmetric units in a single particle reconstruction that contribute to a cryo-EM model. Despite the lower resolution, tremendous insight may still be gained from the cellular context as evidenced by the two cryo-ET examples presented here.

Both cryo-EM and cryo-ET offer unique views of nanomachines, and as such integrating the two approaches can generate multi-resolution models where a tomogram establishes a low-resolution survey of a cell, and the individual machines in that model are the product of cryo-EM studies. This integrated approach is demonstrated in our last example.

#### 3.1 Skeletal Muscle Calcium Release Channel

Ryanodine receptor (RyR1) is a 2.3 MDa homotetramer that regulates the release of  $\text{Ca}^{2+}$  from the sarcoplasmic reticulum to initiate muscle contraction (reviewed in [46]). Figure 2A shows the 9.6Å resolution cryo-EM density map of RyR1 reconstructed from ~28,000 particle images (Figure 2B) [47]. In this map, the structural organization, including the transmembrane and cytoplasmic regions for each monomer, as well as domains within individual monomers can be clearly seen.

Structural analysis of the RyR1 map using SSEHunter [48] revealed 41  $\alpha$ -helices, 36 in the cytoplasmic region and 5 in the transmembrane region, as well as 7  $\beta$ -sheets in the cytoplasmic region of a RyR1 monomeric subunit (Figure 2C). Interestingly, a kinked inner, pore lining helix and a pore helix in the transmembrane region bears a remarkable similarity to those of the MthK channel [67].  $\beta$ -sheets located in the constricted part that connect the transmembrane and cytoplasmic regions have been seen in the crystal structures of inward rectifier K<sup>+</sup> channels (Kir channels) [68, 69] and a cyclic nucleotide-modulated (HCN2) channel [70]. In Kir channels, this  $\beta$ -sheet has been proposed to form a part of the cytoplasmic pore, which is connected to the inner pore. Therefore, this region in the RyR1 may play a role in regulating the ions by interacting with cellular regulators which are yet to be determined.

While there is no crystal structure from any domain or region of RyR1, a homologous domain from the IP<sub>3</sub> receptor is known. Using the aforementioned cryo-EM constrained homology modeling approach [38], it was possible to derive three protein folds, based on the ligand-binding suppressor and IP<sub>3</sub>-binding core domains from the type 1 IP<sub>3</sub> receptor, for the N-terminal portion (residues 12-565) of the RyR1 primary sequence [49] (Figure 2D). Interestingly, these models were localized to a region at the four corners of the RyR1 tetramer, a region that has also been implicated to interact with the DHPR during the excitation-contraction coupling of the muscle [72-74]. Also of interest, several disease related mutations in RyR1 occur within this region. As such, imaging of RyR1 with cryo-EM coupled to structural analysis has resulted into insight into the channels function and role in muscle contraction.

### 3.2 Bacteriophage Epsilon15

Epsilon15 is a 700Å wide, 22 MDa nanomachine that infects salmonella (Figure 3A) [50]. An icosahedral protein shell surrounds its dsDNA genome; at one vertex a large tail assembly protrudes from this shell. Without imposing any symmetry, a reconstruction of the native virion revealed at ~20 Å resolution all the molecular components of the virus including the portal vertex (Figure 3B) [50]. When icosahedral symmetry was imposed during the reconstruction (effectively increasing the number of particle images as there

are 60 asymmetric units per particle), features of the non-icosahedral components such as the portal vertex were averaged out but the icosahedral position shell proteins could be seen at a finer detail (4.5Å resolution) [15]. In this high-resolution map, a complete annotation of the capsid components was possible.

While ~4.5Å resolution is generally insufficient to construct a model by X-ray crystallographic standards, the aforementioned *de novo* model building tools for cryo-EM density maps make it possible with the existence of large  $\alpha$ -helices which can be used to anchor the sequence-to-structure assignment. Gp7, a 420 amino acid protein that makes up the majority of the icosahedral capsid shell, was identified in the reconstruction and shown to have eight  $\alpha$ -helices (>2.5 turns) and three  $\beta$ -sheets. Using these features, a complete *de novo* model was constructed (Figure 3C) revealing a structure similar to that of the HK97 major capsid protein [51] despite the lack of detectable sequence similarity. In addition to the detection of a common fold, side chain density could also be visualized in several regions throughout the map (Figure 3D).

Construction of the Gp7 model clearly revealed the presence of a previously undetected capsid protein. Biochemical analysis of the capsid later confirmed this protein to be Gp10 (12 kDa). In analyzing the sequence of this protein, potential structural homology to PDZ domains [77] was identified. Taken together with the location of this protein of the capsid surface (along the icosahedral two-fold symmetry axes), this small protein likely acts like a molecular staple bridging four adjacent gp10 molecules and thus assuring stability in the mature capsid (Figure 3E).

### 3.3 Bacterial Flagellum

The bacterial flagellum is an intricate biological nanomachine that transduces chemical energy into mechanical. The flagellar motor is a complicated assembly of approximately 25 unique polypeptide components that, when assembled correctly and operating under the proper electrochemical gradient, drives the rotary motor at speeds of nearly 300Hz (reviewed in [52]). Models of the flagellar motor have been advanced through both single particle and helical cryo-EM studies of the purified complexes from various spirochetes [53-55]. Cryo-ET has been used to complement these models; the *in situ* perspective

derived from tomograms can reveal components of the structure that may be—and if fact, are—lost in the isolation and purification steps.

Recent work has utilized cryo-ET to examine *in situ* the structure of the motor and the greater flagellar apparatus from spirochete *Treponema primitia*. In their first report, Jensen and coworkers present the structural details of the motor [56] in which twenty flagellar motors were computationally isolated from their positions in the cryo-ET reconstructions of 15 intact cells (each cell has two flagella, but not all tomograms captured both). These motors were subsequently merged to yield a  $\sim 70\text{\AA}$  resolution model (Figure 4A). Like manmade motors, the flagellar motor consists of a rod attached to a rotor that rotates amidst an array of stationary stators; purified flagellar complexes lacked the stators altogether. This tomography-derived model was the first reconstruction to integrate the full motor with the stators, revealing the stators' 16-fold symmetry and their position with respect to the membrane. Besides accounting for the stator density, this model also revealed unexpected density above the stators in the peptidoglycan layer, including a new component termed the P-collar (Figure 4B). The P-collar and new findings about stator geometry raise new questions about the motor's mechanistic details.

A second report by Jensen and coworkers reveals a plethora of novel structures in the *Treponema* cell: outer-membrane bowls, polar fibrils, a polar cone, and a surface hook arcade that sometimes tracks with the cellular position of flagella (Figure 4C, 4D) [57]. These findings beg new questions as to how and if these features relate to flagellar function. More importantly, two distinct periplasmic layers in *T. primitia* were revealed; this observation, when combined with video observations by light microscopy, affirms the rolling cylinder model of motility over the competing gyration model. The importance of this motility mechanism is underscored by the association between motility and pathogenicity in spirochetes such as those that cause Lyme disease and Syphilis (reviewed in [58]).

### 3.4 Proteomic Atlas

Traditional cellular biology studies are frequently limited by carrying out experiments *in vitro* or investigating only fractions of cells. It is an obvious and tremendous advantage

to integrate the structures and processes of all of the cellular space, enabling investigators to comprehend cells *in toto*. Baumeister and colleagues are making strides towards this goal of visualizing a complete cell with all of its major nanomachines. Early proof-of-concept studies showed it was possible to identify and differentiate large complexes in tomograms of synthetic cells [6]. Recent advances in data processing suggest that even similar assemblies with subtle differences in mass, such as GroEL and GroEL-GroES, can be differentiated [59]. The first application of mapping nanomachines in a cell demonstrated that the total spatial distribution of ribosomes through an entire cell could be directly observed in spirochete *Spiroplasma melliferum* (Figure 5)[60].

The archaeobacteria *Thermoplasma acidophilum* is a relatively simple cell with only approximately 1507 ORFs comprising considerably fewer subcellular assemblies [61]. As such it is an attractive cryo-ET target for mapping the 3D position of all major nanomachines—the proteomic atlas. This atlas will ultimately reveal unprecedented detail about the 3D organization of protein-protein networks [62].

#### 4. FUTURE PROSPECTS

Single particle cryo-EM has reached the turning point at which it is now possible to resolve relatively high-resolution structures of molecular nanomachines under conditions not generally possible with other high-resolution structure determination technique. Due to the intrinsic nature of the cryo-EM experiment, it can also produce unique and biologically important information even when a high-resolution structure is already known. Cryo-EM structures of both the ribosome [78] and GroEL [14, 79, 80] have provided significant insight into structural and functional mechanisms despite being extensively studied using X-ray crystallography.

An obvious challenge for cryo-EM is the pursuit of higher resolution (i.e. close to or better than 3.0Å), at which point full, all atom models could be constructed. On the other hand, cryo-EM is not just aimed at high resolution. Cryo-EM offers the ability to resolve domains and/or components that are highly flexible at lower resolutions, as well as samples with multiple conformational states [63]. With further developments in the image processing routines, both high-resolution structure determination and

“computational purification” of samples [63] will further allow for the exploration of complex molecular nanomachines in greater detail.

Like cryo-EM, improvements in data collection and image processing will allow cryo-ET to achieve more accurate and higher resolution reconstructions of large nanomachines and cells. However, as alluded to in the proteomic atlas, the real strength of cryo-ET is its power to integrate known atomic structures and cryo-EM reconstructions to provide a complete model of *in vivo* protein function [62, 64]. Such integration will ultimately establish a true spatial and temporal view of functional nanomachines within the cell, which can systematically be investigated in either healthy or diseased states. In addition, there is a trend towards the integration of live cell observations made by light microscopy followed by cryo-ET observations of the same specimens [65]. Such hybrid approaches require both new instrumentation to make sequential observations practical and the computational tools to integrate the data. These integrated cellular views promise to enhance our understanding of cell structure and function relationships at higher spatial and temporal resolutions.

**Acknowledgements:** This research has been supported by grants from NIH (P41RR02250, 2PN2EY016525, R01GM079429) and NSF (IIS-0705474, IIS-0705644). We thank our collaborators Drs. Irina Serysheva, Steve Ludtke, Yao Cong, Maya Topf, Andrej Sali and Susan Hamilton on the RYR1 project; Wen Jiang, Peter Weigele, Jonathan King, Joanita Jakana and Juan Chang on the epsilon15 phage project; Jose Lopez on human platelet. We thank Dr. Grant Jensen at California Institute of Technology and Drs. Wolfgang Baumeister and Julio Ortiz at Max Planck Institute for providing the art for figures 3 and 4, respectively.

## FIGURE CAPTIONS

**Figure 1.** The experimental pipeline for cryo imaging experiments is depicted. (A) The first steps of the experiment--specimen preparation, specimen freezing, and microscopy--are common to both cryo-EM and cryo-ET. (B) The subsequent steps diverge and differ between the two types of experiments. For cryo-EM these steps are illustrated with examples of the biological nanomachine GroEL. For cryo-ET these steps are illustrated with a cell, the human platelet.

**Figure 2.** RyR1 at 9.6Å resolution [49]. RyR1 at 9.6Å resolution (side and top views shown in A) were reconstructed from ~28,000 individual particle images. The four subunits are annotated in different colors. A representative view of particle images is shown in (B). The spatial dispositions of the  $\alpha$ -helices (cylinders) and  $\beta$ -sheets (orange planes) in two of the homotetrameric subunits are shown in (C). The three N-terminal models for RyR1 are shown fit to the cryo-EM density map in (D). Model 1 is shown in cyan (residues Q12-S207), model 2 is shown in yellow (residues G216-T407) and model 3 is shown in red (residues A408-Y565). Model 2 and 3 are based on the aforementioned IP3-binding core domain, while model 1 is based on the ligand-binding suppressor domain.

**Figure 3.** Bacteriophage epsilon15 (a) 300-kV electron image of the phage particles embedded in vitreous ice is shown in (A). A cut-away view of the 20Å asymmetric reconstruction of epsilon15 [50] shows the molecular components of the portal vertex, the capsid shell protein and the viral DNA are shown in (B). Different molecular components are annotated in different colors. (C) In the 4.5Å resolution structure [15], the backbone model of the Gp7 and the density of Gp10 can be seen. Side-chain density in the cryo-EM map can be seen in (D). In (E), a zoomed-in view of the capsid shows one gp10 spanning across 4 gp7 molecules, functioning as a molecular stapler.

Figure 4: Cryo-ET findings on the flagellar motor and cellular features of spirochete *Treponema primitia*. (A), A cutaway surface rendering of the flagellar motor computed by averaging together 20 motors computationally isolated from tomograms. Novel

findings include the surprising connectivity between the stator and other components of the motor, marked by yellow arrows. (B), Schematic of the motor organization as revealed through the analysis of the structure shown in A. The position and geometry of the stator and the existence of the P-collar were missed by previous studies that looked at biochemically purified flagellar motors. (C), Surface rendering of a *T. primitia* cell where many novel cellular structures are shown: surface bowls in magenta, surface hook arcade in yellow and tip fibrils in orange; flagella are in green and red.

Figure 5. A map of ribosome location in the spirochete *Spiroplasma melliferum*. (A) The 0° projection, an unprocessed cryo-ET image, showing a spirochete cell. (B) A slice of the reconstruction, which shows higher density at positions occupied by ribosomes. (C) A surface rendering of the reconstruction which has been filtered and segmented. High confidence ribosome matches are colored green; intermediate confidence matches are colored yellow.

## REFERENCES

- [1] A. C. Martin, D. G. Drubin, *Curr Opin Cell Biol* **2003**, *15*, 6.
- [2] H. M. Berman, J. Westbrook, Z. Feng, G. Gilliland, T. N. Bhat, H. Weissig, I. N. Shindyalov, P. E. Bourne, *Nucleic Acids Res* **2000**, *28*, 235.
- [3] R. M. Glaeser, K.H. Downing, D. DeRosier, W. Chiu and J. Frank, *Electron crystallography of biological macromolecules*, Oxford University Press, Oxford ; New York, **2007**.
- [4] J. Frank, *Three-dimensional electron microscopy of macromolecular assemblies : visualization of biological molecules in their native state*, [2nd ed., Oxford University Press, New York, **2006**.
- [5] J. Dubochet, M. Adrian, J. J. Chang, J. C. Homo, J. Lepault, A. W. McDowell, P. Schultz, *Q Rev Biophys* **1988**, *21*, 129.
- [6] A. S. Frangakis, J. Bohm, F. Forster, S. Nickell, D. Nicastro, D. Typke, R. Hegerl, W. Baumeister, *Proc Natl Acad Sci U S A* **2002**, *99*, 14153.

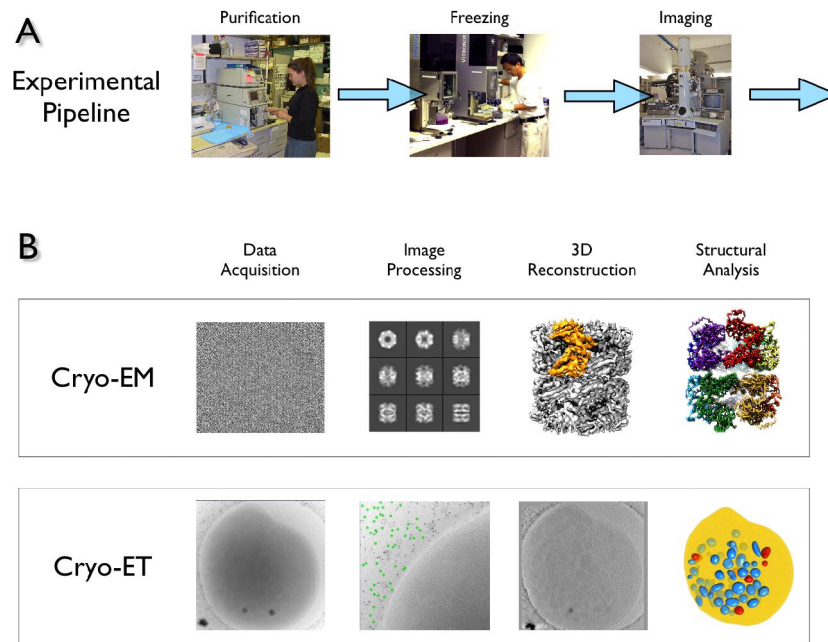
- [7] R. Grimm, H. Singh, R. Rachel, D. Typke, W. Zillig, W. Baumeister, *Biophys J* **1998**, *74*, 1031.
- [8] S. Nickell, R. Hegerl, W. Baumeister, R. Rachel, *J Struct Biol* **2003**, *141*, 34.
- [9] P. M. Frederik, D. H. Hubert, *Methods Enzymol* **2005**, *391*, 431.
- [10] H. D. White, M. L. Walker, J. Trinick, *J Struct Biol* **1998**, *121*, 306.
- [11] K. Murata, K. Mitsuoka, T. Hirai, T. Walz, P. Agre, J. B. Heymann, A. Engel, Y. Fujiyoshi, *Nature* **2000**, *407*, 599.
- [12] R. Henderson, J. M. Baldwin, T. A. Ceska, F. Zemlin, E. Beckmann, K. H. Downing, *Biochem Soc Trans* **1990**, *18*, 844.
- [13] A. Miyazawa, Y. Fujiyoshi, N. Unwin, *Nature* **2003**, *424*, 949.
- [14] K. Yonekura, S. Maki-Yonekura, K. Namba, *Nature* **2003**, *424*, 643.
- [15] W. Jiang, M. L. Baker, J. Jakana, P. R. Weigele, J. King, W. Chiu, *Nature* **2008**, *451*, 1130.
- [16] S. J. Ludtke, M. L. Baker, D. H. Chen, J. L. Song, D. T. Chuang, W. Chiu, *Structure* **2008**, *16*, 441.
- [17] L. R. Comolli, K. H. Downing, *J Struct Biol* **2005**, *152*, 149.
- [18] C. V. Iancu, W. F. Tivol, J. B. Schooler, D. P. Dias, G. P. Henderson, G. E. Murphy, E. R. Wright, Z. Li, Z. Yu, A. Briegel, L. Gan, Y. He, G. J. Jensen, *Nat Protoc* **2006**, *1*, 2813.
- [19] E. R. Wright, C. V. Iancu, W. F. Tivol, G. J. Jensen, *J Struct Biol* **2006**, *153*, 241.
- [20] D. L. DeRosier, A. Klug, *Nature* **1968**, *217*, 130.
- [21] R. A. Crowther, DeRosier, D.J., Klug, A., *Proceedings of the Royal Society of London* **1970**, *317*, 319.
- [22] R. Henderson, *Quart Rev Biophys* **2004**, *37*, 3.
- [23] S. J. Ludtke, P. R. Baldwin, W. Chiu, *J Struct Biol* **1999**, *128*, 82.
- [24] J. Frank, M. Radermacher, P. Penczek, J. Zhu, Y. Li, M. Ladjadj, A. Leith, *J Struct Biol* **1996**, *116*, 190.
- [25] M. van Heel, G. Harauz, E. V. Orlova, R. Schmidt, M. Schatz, *J Struct Biol* **1996**, *116*, 17.
- [26] N. Grigorieff, *J Struct Biol* **2007**, *157*, 117.
- [27] W. O. Saxton, W. Baumeister, *J Microsc* **1982**, *127*, 127.

- [28] M. C. Lawrence, in *Electron Tomography: Three-dimensional Imaging with the Transmission Electron Microscope*, First ed. (Ed.: J. Frank), Springer, **1992**, pp. 197.
- [29] P. K. Luther, M. C. Lawrence, R. A. Crowther, *Ultramicroscopy* **1988**, *24*, 7.
- [30] D. N. Mastronarde, in *Electron tomography: Methods for three-dimensional visualization of structures in the cell*, Second ed. (Ed.: J. Frank), Springer, **2006**, pp. 187.
- [31] M. Radermacher, in *Electron tomography: Methods for three-dimensional visualization of structures in the cell*, Second ed. (Ed.: J. Frank), Springer, **2006**, pp. 245.
- [32] K. Sandberg, D. N. Mastronarde, G. Beylkin, *J Struct Biol* **2003**, *144*, 61.
- [33] J. R. Kremer, D. N. Mastronarde, J. R. McIntosh, *J Struct Biol* **1996**, *116*, 71.
- [34] S. Nickell, F. Forster, A. Linaroudis, W. D. Net, F. Beck, R. Hegerl, W. Baumeister, J. M. Plitzko, *J Struct Biol* **2005**, *149*, 227.
- [35] H. Winkler, *J Struct Biol* **2007**, *157*, 126.
- [36] S. Q. Zheng, B. Keszthelyi, E. Branlund, J. M. Lyle, M. B. Braunfeld, J. W. Sedat, D. A. Agard, *J Struct Biol* **2007**, *157*, 138.
- [37] G. Cardone, K. Grunewald, A. C. Steven, *J Struct Biol* **2005**, *151*, 117.
- [38] M. Topf, M. L. Baker, M. A. Marti-Renom, W. Chiu, A. Sali, *J Mol Biol* **2006**, *357*, 1655.
- [39] M. L. Baker, W. Jiang, W. J. Wedemeyer, F. J. Rixon, D. Baker, W. Chiu, *PLoS Comput Biol* **2006**, *2*, e146.
- [40] M. L. Baker, W. Jiang, B. R. Bowman, Z. H. Zhou, F. A. Quioco, F. J. Rixon, W. Chiu, *J Mol Biol* **2003**, *331*, 447.
- [41] M. L. Baker, W. Jiang, F. J. Rixon, W. Chiu, *J Virol* **2005**, *79*, 14967.
- [42] K. Sandberg, in *Cellular electron microscopy* (Ed.: J. R. McIntosh), Elsevier, New York, **2007**, pp. 770.
- [43] F. Forster, R. Hegerl, in *Cellular electron microscopy* (Ed.: J. R. McIntosh), Elsevier, New York, **2007**, pp. 742.
- [44] S. J. Ludtke, L. Nason, H. Tu, L. Peng, W. Chiu, *Microscopy and Microanalysis* **2003**, *9*, 556.

- [45] S. D. Fuller, *Structure (Camb)* **2003**, *11*, 11.
- [46] Serysheva, II, W. Chiu, S. J. Ludtke, *Methods Cell Biol* **2007**, *79*, 407.
- [47] S. J. Ludtke, Serysheva, II, S. L. Hamilton, W. Chiu, *Structure (Camb)* **2005**, *13*, 1203.
- [48] M. L. Baker, T. Ju, W. Chiu, *Structure* **2007**, *15*, 7.
- [49] I. I. Serysheva, S. J. Ludtke, M. L. Baker, Y. Cong, M. Topf, D. Eramian, A. Sali, S. L. Hamilton, W. Chiu, *Proc Nat Acad Sci USA* **2008**, in press.
- [50] W. Jiang, J. Chang, J. Jakana, P. Weigele, J. King, W. Chiu, *Nature* **2006**, *439*, 612.
- [51] W. R. Wikoff, L. Liljas, R. L. Duda, H. Tsuruta, R. W. Hendrix, J. E. Johnson, *Science* **2000**, *289*, 2129.
- [52] H. C. Berg, *Annu Rev Biochem* **2003**, *72*, 19.
- [53] D. R. Thomas, N. R. Francis, C. Xu, D. J. DeRosier, *J Bacteriol* **2006**, *188*, 7039.
- [54] H. Suzuki, K. Yonekura, K. Namba, *J Mol Biol* **2004**, *337*, 105.
- [55] N. R. Francis, G. E. Sosinsky, D. Thomas, D. J. DeRosier, *J Mol Biol* **1994**, *235*, 1261.
- [56] G. E. Murphy, J. R. Leadbetter, G. J. Jensen, *Nature* **2006**, *442*, 1062.
- [57] G. E. Murphy, E. G. Matson, J. R. Leadbetter, H. C. Berg, G. J. Jensen, *Mol Microbiol* **2008**, *67*, 1184.
- [58] R. Lux, A. Moter, W. Shi, *J Mol Microbiol Biotechnol* **2000**, *2*, 355.
- [59] F. Forster, S. Pruggnaller, A. Seybert, A. S. Frangakis, *J Struct Biol* **2008**, *161*, 276.
- [60] J. O. Ortiz, F. Forster, J. Kurner, A. A. Linaroudis, W. Baumeister, *J Struct Biol* **2006**, *156*, 334.
- [61] N. Sun, F. Beck, R. W. Knispel, F. Siedler, B. Scheffer, S. Nickell, W. Baumeister, I. Nagy, *Mol Cell Proteomics* **2007**, *6*, 492.
- [62] C. V. Robinson, A. Sali, W. Baumeister, *Nature* **2007**, *450*, 973.
- [63] D. H. Chen, J. L. Song, D. T. Chuang, W. Chiu, S. J. Ludtke, *Structure* **2006**, *14*, 1711.
- [64] S. Nickell, C. Kofler, A. P. Leis, W. Baumeister, *Nat Rev Mol Cell Biol* **2006**, *7*, 225.

- [65] A. Sartori, R. Gatz, F. Beck, A. Rigort, W. Baumeister, J. M. Plitzko, *J Struct Biol* **2007**, *160*, 135.

For Peer Review



201x155mm (200 x 200 DPI)

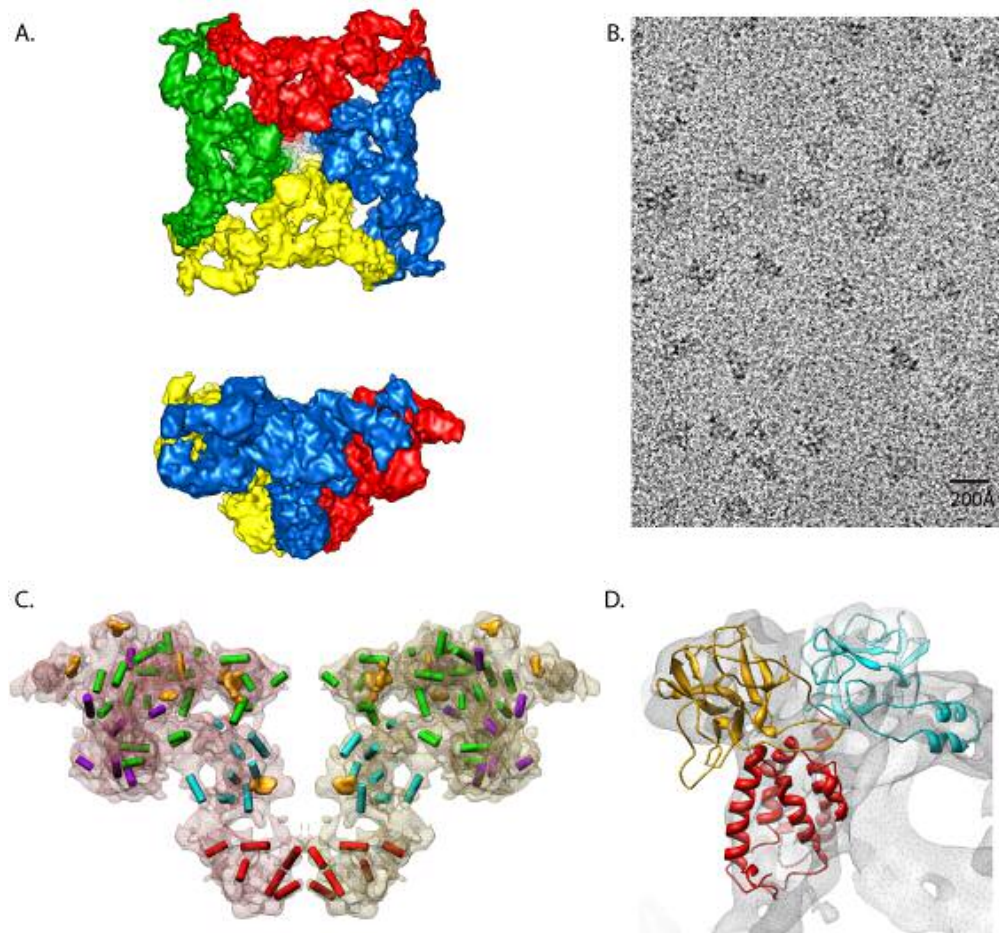


**Figure 2. RyR1 at 9.6Å resolution [71]. RyR1 at 9.6Å resolution (side and top views shown in A) were reconstructed from ~28,000 individual particle images. The four subunits are annotated in different colors. A representative view of particle images is shown in (B). The spatial dispositions of the  $\alpha$ -helices (cylinders) and  $\beta$ -sheets (orange planes) in two of the homotetrameric subunits is shown in (C). The three N-terminal models for RyR1 are shown fit to the cryo-EM density map in (D). Model 1 is shown in cyan (residues Q12-S207), model 2 is shown in yellow (residues G216-T407) and model 3 is shown in red (residues A408-Y565). Model 2 and 3 are based on the aforementioned IP3-binding core domain, while model 1 is based on the ligand-binding suppressor domain.**

143x134mm (100 x 100 DPI)

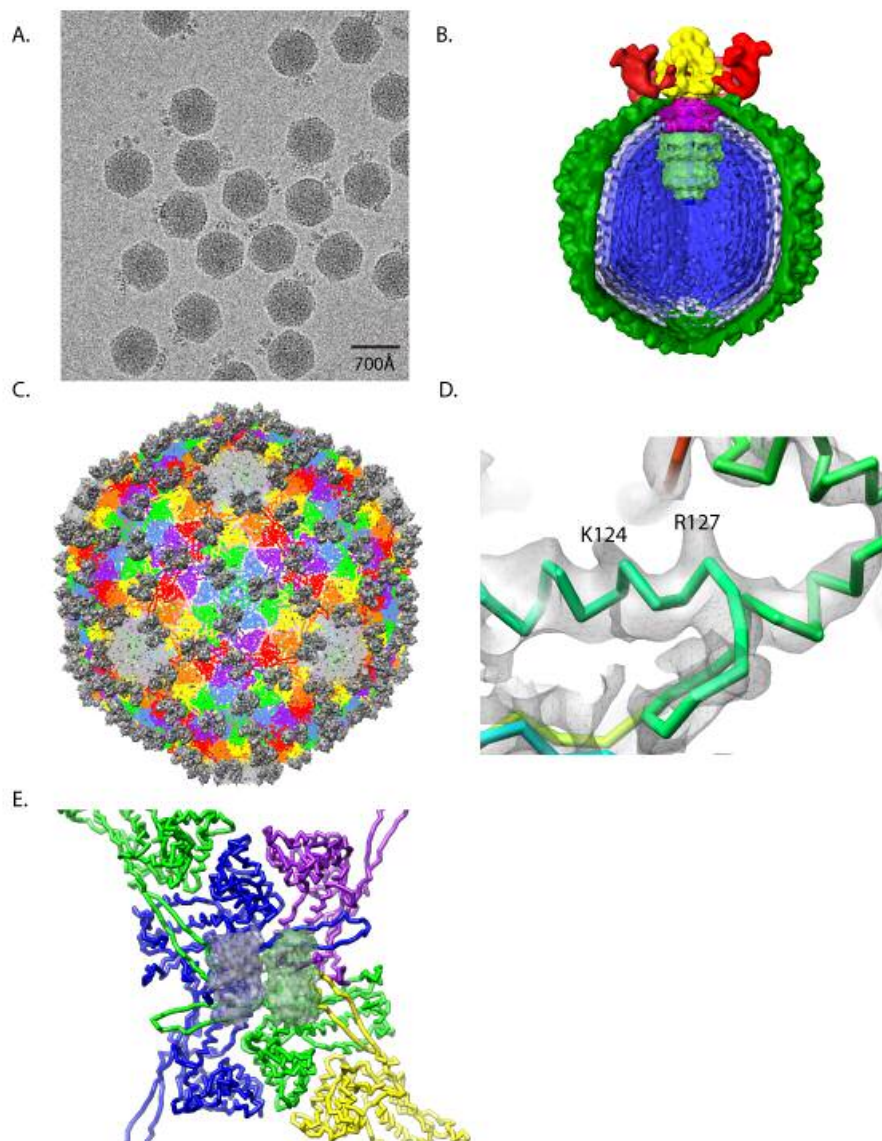
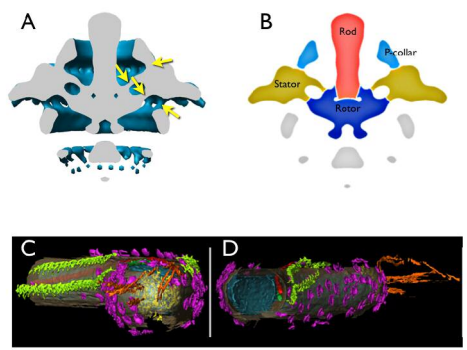


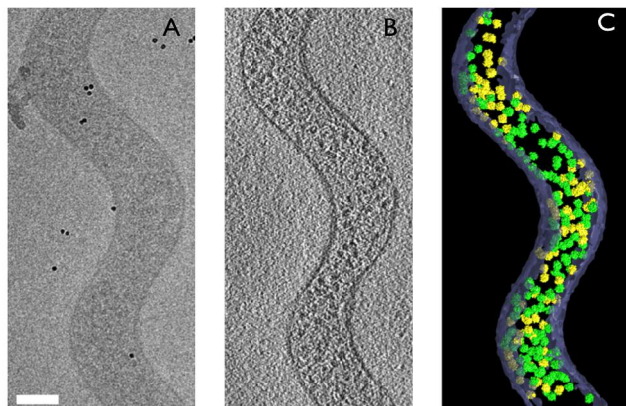
**Figure 3. Bacteriophage epsilon15 (a) 300-kV electron image of the phage particles embedded in vitreous ice is shown in (A). A cut-away view of the 20Å asymmetric reconstruction of epsilon15 [75] shows the molecular components of the portal vertex, the capsid shell protein and the viral DNA are shown in (B). Different molecular components are annotated in different colors. (C) In the 4.5Å resolution structure [13], the backbone model of the Gp7 and the density of Gp10 can be seen. Side-chain density in the cryo-EM map can be seen in (D). In (E), a zoomed-in view of the capsid shows one gp10 spanning across 4 gp7 molecules, functioning as a molecular stapler.**

152x190mm (100 x 100 DPI)



201x155mm (200 x 200 DPI)

Review



201x155mm (200 x 200 DPI)

review